

See discussions, stats, and author profiles for this publication at: <https://www.researchgate.net/publication/263946246>

# Tuning the Performance of Low-Pt Polymer Electrolyte Membrane Fuel Cell Electrodes Derived from Fe<sub>2</sub>O<sub>3</sub>@Pt/C Core–Shell Catalyst Prepared by an in Situ Anchoring Strategy

ARTICLE *in* THE JOURNAL OF PHYSICAL CHEMISTRY C · MARCH 2012

Impact Factor: 4.77 · DOI: 10.1021/jp300628j

---

CITATIONS

16

READS

25

---

## 2 AUTHORS:



Vishal Mahesh Dhavale

Tokyo Institute of Technology

15 PUBLICATIONS 128 CITATIONS

[SEE PROFILE](#)



Sreekumar Kurungot

CSIR - National Chemical Laboratory, Pune

112 PUBLICATIONS 1,389 CITATIONS

[SEE PROFILE](#)

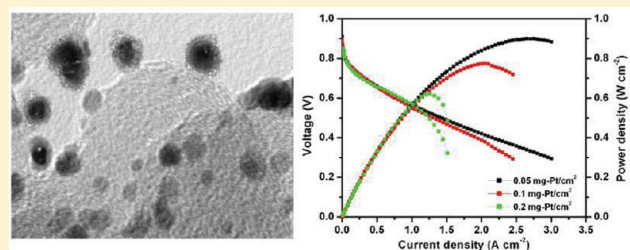
# Tuning the Performance of Low-Pt Polymer Electrolyte Membrane Fuel Cell Electrodes Derived from $\text{Fe}_2\text{O}_3@\text{Pt/C}$ Core–Shell Catalyst Prepared by an in Situ Anchoring Strategy

Vishal M Dhavale and Sreekumar Kurungot\*

Physical and Materials Chemistry Division, National Chemical Laboratory, Pune 411008, India

## Supporting Information

**ABSTRACT:** A low-Pt electrode with high performance and durability characteristic has been realized for polymer electrolyte membrane fuel cell applications from a carbon-supported  $\text{Fe}_2\text{O}_3@\text{Pt/C}$  core–shell catalyst prepared by a process involving in situ surface modification-cum-anchoring strategy. The process is based on an in-house-developed methodology for generating and interlocking the core–shell nanoparticles on the surface of the carbon substrate, which undergoes functionalization in the reaction medium itself by the intervention of the reducing agent employed in the reaction. Ascorbic acid, which was used as the reducing agent in the process, played a crucial role by making use of its multifunctional activities as reducing agent, stabilizing agent, as well as capping agent in addition to its efficiency in functionalizing the carbon surface during the course of the reaction. The formation of core–shell nanostructures could be confirmed by XRD, HR-TEM, and cyclic voltammetric analysis. The oxygen reduction property and the performance during the single cell evaluations were found to be strongly influenced by the thickness of the catalyst layer owing to the ohmic contribution from the higher mass fraction of the less conductive  $\text{Fe}_2\text{O}_3$  core. However, when the thickness of the catalyst layer was kept within the threshold level,  $\text{Fe}_2\text{O}_3@\text{Pt}$  catalyst clearly outperforms the commercial Pt/C catalyst. This benefit of the core–shell catalyst enabled it to display a maximum power density of  $900 \text{ mW/cm}^2$  with a significantly low cathode Pt loading of  $0.05 \text{ mg/cm}^2$ . An accelerated durability assessment of the membrane electrode assembly for 10 h gave consistent performance characteristics. The study gave convincing evidence on the feasibility of using the electrodes derived from the core–shell catalyst prepared by the in situ anchoring strategy for developing cost competitive systems and miniature cells for niche applications.



## 1. INTRODUCTION

Currently, immense research is being carried out to realize the ultimate solution to the world's energy demands, and polymer electrolyte membrane fuel cell (PEMFCs) stand out as one of the most promising candidates, as it ensures green energy under commercially easily viable operating conditions. Due to prominent features like high energy density, relatively low operating temperatures, zero or low emission, and minimal corrosion problems, PEMFCs are acclaimed as one of the best solutions for a variety of technocommercial applications in a situation where requirements for performance and emission cannot be compromised. Unfortunately, in spite of these advantages of the system and advancements in the developments of materials, components, and technology, the cost and durability of Pt-based electrodes act as the major stumbling blocks for PEMFCs to find their way into the energy market. Moreover, irrespective of the high energy efficiencies expected from the thermodynamic point of view, in the practical operation of PEMFCs, the activation and mass-transfer losses significantly reduce the overall efficiency of the system.

Reduction in the activation, concentration, and ohmic overvoltages will have a significant impact in narrowing down the gap between the thermodynamic and experimental

performance characteristics of a PEMFC. This involves requirements of highly efficient oxygen reduction catalysts owing to the high overpotential associated with the reaction and complementary processes for electrode fabrication and system integration by properly minimizing the performance losses associated with ohmic and mass-transfer components. Maximizing the exchange current density is a viable way to reduce the activation losses. Since the exchange current density is a function of the catalyst material, surface roughness, and its structure, there have been extensive efforts on the improvement of catalyst-electrode design and enhancement of active sites.<sup>1</sup> In order to deploy PEMFCs for automotive and stationary applications, researchers still prefer to maintain high Pt loadings as there is no other practical way to simultaneously maintain sustainable performance especially in the context of the obtainable Pt utilization of only 25–30% reported in the literature.<sup>1</sup> This consequently leads to thicker electrodes, thereby further decreasing the overall Pt utilization.<sup>2</sup> DOE set a target of  $0.3 \text{ mg/cm}^2$  for 2010 and  $0.2 \text{ mg/cm}^2$  for 2015.<sup>3</sup>

**Received:** January 18, 2012

**Revised:** March 9, 2012

**Published:** March 9, 2012

However, there is another sector involving portable devices where miniature fuel cells with responsive thin and small-sized electrodes have distinct benefits. This necessitates high Pt utilization, reducing ohmic overvoltage, and activity characteristics, all the while keeping the electrode layer as thin as possible to enable tangible system integration.<sup>4</sup> However, electrodes based on conventional Pt/C catalysts below a threshold thickness level generally fail to deliver required power outputs due to the poor obtainable utilization level of Pt in most of these systems.<sup>5</sup>

One strategy being adopted to reduce the electrode thickness is to fabricate electrodes from Pt/C catalyst containing significantly higher loading of Pt because the required Pt loading can be achieved by simultaneously avoiding significant carbon content in the electrode. However, close proximity and relatively dense dispersion of Pt nanoparticles on such catalysts make the systems more prone to degradation due to sintering and carbon corrosion. Two other strategies adopted to simultaneously address the cost and performance requirements are by adopting innovative strategies for increasing Pt utilization and by creating overlayer structures during electrode fabrication. Great efforts have been made in this direction by synthesizing bimetallic and multimetallic heterogeneous catalysts.<sup>4</sup> In bimetallic systems, mainly three fundamental effects could be observed, i.e., *ensemble*, *ligand*, and *geometric* effects.<sup>6</sup> The first one is due to the involvement of desperate surface atoms to take on distinct functionalities. The ligand effect occurs when two dissimilar surface neighborhood atoms induce electronic charge transfer between the atoms, which eventually leads to change in the electronic band structure of the interacting atoms.<sup>7</sup> The geometric effect implies differences in reactivity based on the atomic arrangement of surface atoms, which is expected to include compressed or expanded arrangements of surface atoms termed as surface strain.<sup>7</sup> Pt based core–shell structured systems are exceptionally important in this context due to the coexistence of all the aforementioned three favorable effects in modulating the property characteristics and thereby enhancing the oxygen reduction abilities. There is ample evidence that core metals such as Cu and Fe lower the d-band of the shell with respect to the Fermi level, making oxygen reduction by the Pt-shelled particles more feasible compared to that of bulk Pt nanoparticles.<sup>8</sup> While both ligand and strain effects determine the d-band center of the Pt shell, a greater surface relaxation reduces the strain in nanoparticles as compared to single crystal near-surface alloys. Thus, addition of non-noble metal can change the geometric as well as electronic structure of Pt, which ultimately enhances its activity and utilization during oxygen reduction reaction (ORR).<sup>5,9</sup>

The feasibility of achieving Pt in the form of monolayer in Pt-based core–shell systems essentially decreases the amount of Pt to be loaded in the system while the non-noble metal core modifies the electronic environment of Pt by reducing the interatomic distances.<sup>8,9</sup> Overall, Pt in the form of a thin shell on non-noble metal core leads to enhanced catalyst utilization, better efficiency, and higher catalytic activity, thus giving immense scope for validating the techno-commercial prospects of PEMFC by utilizing this new class of materials. However, the ability to fabricate core–shell particles with uniform thickness, controllable composition, and uniform dispersion on a support is really a challenging task. Herein, we synthesized carbon-supported  $\text{Fe}_2\text{O}_3@\text{Pt}$  core–shell nanoparticles ( $\text{Fe}_2\text{O}_3@\text{Pt/C}$ ) by adopting a simple reduction-cum-anchoring method, which

helps to simultaneously meet the essential requirements with respect to size, structure, dispersion, and cost of the active component in the electrode. The basic theme of the work involves direct interlocking of the core–shell nanoparticles as and when they are formed on the surface of the substrate surface which undergoes *in situ* functionalization during the course of the reaction by the intervention of the reducing agent and its degradation products.<sup>10</sup> Thus, both the core–shell feature and dispersion could be simultaneously maintained. Most importantly, under ultralow Pt loading conditions, it has been observed that the electrodes derived from the core–shell catalyst outperform the conventional Pt/C catalyst. This outstanding performance of the electrodes formed from the  $\text{Fe}_2\text{O}_3@\text{Pt/C}$  catalyst opens up a great scope for realizing cost-effective systems and miniature cells for various niche applications.

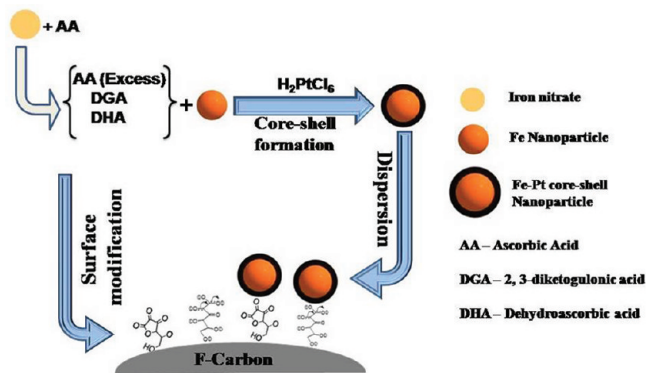
## 2. EXPERIMENTAL SECTION

**Materials and Methods.**  $\text{Fe}(\text{NO}_3)_3 \cdot 9\text{H}_2\text{O}$ , ascorbic acid (AA), NaOH, chloroplatinic acid, and hydrogen peroxide were procured from Sigma-Aldrich and used as such without any further purification. Nafion 212 membrane was procured from DuPont and subjected to pretreatment by following a reported procedure.<sup>11</sup>

**Synthesis of Electrocatalyst.** An aqueous solution of  $\text{Fe}(\text{NO}_3)_3$  (0.1 N, 16 mL) was reduced by adding 80 mL of a 0.1 N aqueous solution of AA. The mixture was stirred for 60 min and the pH (pH = 10) of the reaction mixture was maintained by the dropwise addition of a 10% NaOH solution. Once the reduction of iron was over, instantaneously, 16 mL of 0.1 N chloroplatinic acid solution was added without altering the pH of the mixture. The reaction mixture was kept under stirring for 40 min to ensure complete reduction of Pt, as indicated from the color change of the mixture to black. Functionalized carbon (FC) was dispersed in DI water by ultrasonication and instantly added to the reaction mixture, and subsequently, the mixture was kept under stirring for 10 h. All the additions were done with a constant stirring of the reaction mixture. The aging step with the optimized duration of 10 h was found to be very critical to effectively facilitate *in situ* interlocking of the core–shell nanoparticles by the intervention of the moieties created from the reducing agent and the functional groups existing on the carbon surface. The unreacted AA and its oxidized and degradation products were the key mediators in building the interaction between the as formed core–shell nanoparticles and the carbon support. The slurry was filtered through 0.2  $\mu\text{m}$  pore size filter paper and the wet cake was dried at 90 °C for 2 h to get the final material ( $\text{Fe}_2\text{O}_3@\text{Pt/C}$ ). Scheme 1 represents how the direct interlocking process works with the intervention of the species originated during the course of the reaction. The Pt to Fe weight ratio in the reaction mixture was fixed on the basis of an optimization study, and the composition of the reaction mixture as given here was the one giving the well-featured core–shell nanoparticles possessing a continuous Pt shell of minimum possible thickness without any indication of exposed patches of the Fe-based core. The details on the process optimization of the shell thickness complemented by the electrochemical and other characterization methodologies are given in the Supporting Information.

**Characterization.** *Structural Characterization.* A well-dispersed sample for high-resolution transmission electron microscopy (HR-TEM) analysis was prepared by sonicating the

**Scheme 1.** Schematic Representation of the Strategy Involved in the Synthesis of the  $\text{Fe}_2\text{O}_3@\text{Pt/C}$  Core–Shell Nanoparticles by the Sequential Reduction Method



catalyst (1 mg) in 5 mL of 2-propanol solvent. The as prepared sample was drop-coated on a carbon-coated 200 mesh Cu grid and was dried under vacuum, and images were obtained on an FEI, TECNAI G2 F30 instrument operated at an accelerated voltage of 300 kV ( $\text{Cs} = 0.6$  mm, resolution 1.7 Å). The thickness of electrode has been confirmed by using an SEI-Quanta-200 3D dual beam E-SEM with an accelerated voltage of 500 V-30 keV. X-ray diffraction (XRD) patterns were recorded on PANalytical instrument using  $\text{Cu K}\alpha$  radiation ( $\lambda = 1.54$  Å) at a scanning rate of  $2^\circ \text{ min}^{-1}$  and a step size of  $0.02^\circ$  in  $2\theta$ . X-ray photoelectron spectroscopy (XPS) measurements were carried out on a VG Micro Tech ESCA 300° instrument at a pressure of  $>1 \times 10^{-9}$  Torr (pass energy 50 eV, electron takeoff angle  $60^\circ$ , and the overall resolution  $\sim 0.1$  eV). Infrared (IR) spectra were recorded on a Perkin-Elmer instrument. Thermogravimetric experiments (TGA) were carried out in the temperature range from room temperature to  $900^\circ \text{ C}$  on an SDT Q600 TG-DTA analyzer under  $\text{N}_2$  atmosphere.

**Electrochemical Studies.** An Autolab PGSTAT30 (Eco-Chemie) instrument was used to investigate the electrochemical properties by cyclic voltammetry (CV), and rotating disk electrode (RDE) studies in a conventional three-electrode test cell with  $\text{Ag}/\text{AgCl}$  (saturated 3 M KCl) as the reference electrode (RE) and a platinum foil as the counter electrode (CE). For the preparation of the working electrode (WE), the catalyst slurry was made by sonicating 5 mg of the catalyst in 1 mL of a 3:2 EtOH:H<sub>2</sub>O mixture. The catalyst slurry was drop-coated on a previously polished (by using 0.3  $\mu\text{m}$  alumina slurry) glassy carbon (GC) electrode surface (geometrical area = 0.07065 cm<sup>2</sup>) to achieve the required Pt loading, and 2.5  $\mu\text{L}$  of 0.01 wt % Nafion solution was applied on the whole surface of the electrode to yield a uniform thin film. The electrode was dried for 2 h in air and was used as the WE for the electrochemical investigations. An aqueous solution of 0.5 M perchloric acid, deaerated with  $\text{N}_2$  gas, was used as an electrolyte for normal CV and RDE studies. Moreover, to get the mass activity plots, current was divided by the corresponding Pt loading, and all the graphs were further normalized with respect to normal hydrogen electrode (NHE) with 60% IR compensation. For ohmic correction, the resistance was measured by positive feedback method and the resistance contribution was found to be  $350 \Omega^{21}$ .

**Fuel Cell Testing.** To demonstrate the realistic perspective of utilizing the core–shell catalysts with modified ORR properties in the cathode electrodes (where reduction of oxygen occurs)

of the membrane electrode assembly (MEA) of PEMFCs, single cell performance evaluations were carried out. MEAs were prepared by maintaining a constant anode Pt loading of 0.3 mg of Pt/cm<sup>2</sup> of Pt/C and by varying the cathode Pt loading as 0.05, 0.1, and 0.2 mg of Pt/cm<sup>2</sup> using  $\text{Fe}_2\text{O}_3@\text{Pt/C}$  core–shell catalysts by the brushing method. To effectively compare the performance variation, another MEA was prepared by employing Pt/C itself in the cathode side by maintaining a Pt loading of 0.05 mg of Pt/cm<sup>2</sup>. The as prepared Nafion (N-212) based MEAs were tested by FCT test station unit by passing an ultrapure grade fuel (hydrogen) at the anode and oxidant (oxygen) at the cathode side with a flow rate of 0.2 standard liters per minute (slpm) and at 100% relative humidity. To maintain the desired current profile while collecting the lifetime data (durability data), a cyclical current step protocol was written to control the output and load box setting. This protocol was based on the Set Protocol.vi from the FCT test station software library, in which we can specify the current settings of the load box under constant current (CC) mode, as well as the time delay for each of the current setting after the specification has been reached. At the same time, individual test parameters like gas flow rates, current, voltage, and temperatures of the running MEA were examined and documented via an independent Lab-viewfile (Alone LT.vi, from FCT software library) software.

### 3. RESULTS AND DISCUSSION

Figure 1a shows the HR-TEM image of well-dispersed  $\text{Fe}_2\text{O}_3@\text{Pt/C}$  nanoparticles on carbon support. Figure 1b shows the

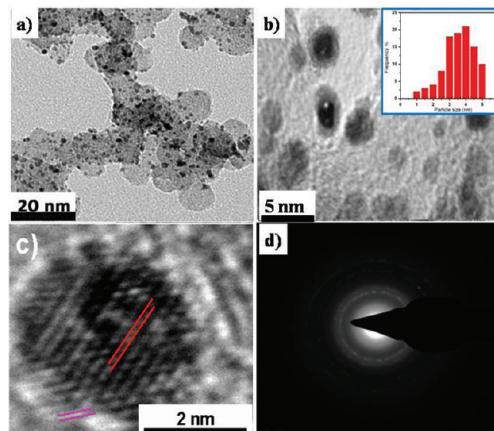


**Figure 1.** TEM images of (a)  $\text{Fe}_2\text{O}_3@\text{Pt/C}$  well-dispersed core–shell nanoparticles on the surface of the carbon support and (b)  $\text{Fe}_2\text{O}_3@\text{Pt/C}$  core–shell nanoparticles clearly showing the boundaries of the core and shell regions of the nanoparticles, where the inset shows the particle size histogram of  $\text{Fe}_2\text{O}_3@\text{Pt/C}$  nanoparticles, indicating an average particles size of  $\sim 3\text{--}5$  nm. (c) HR-TEM image of a single particle showing the lattice mismatch at the edge of the core and shell region. (d) SAED pattern.

highly resolved image with essential features of the core–shell structure. As evident from these images, the core–shell nanoparticles are well-separated from each other and the monodispersity of the nanoparticles is essentially maintained with an average particle size of  $\sim 3\text{--}5$  nm. The particles size histogram (inset of Figure 1b) gives the evidence for the monodispersity of nanoparticles. The magnified image of the single particle with lattice fringes given in Figure 1c reveals

lattice mismatch at the interface of the core and shell. This indicates the formation of crystalline core–shell nanoparticles and moreover it is attributed to the reduction in Pt–Pt interatomic distance at the surface, which eventually helps in improving the ORR activity. The calculated *d*-spacing values from selective area diffraction (SAED, Figure 1d) pattern are 3.35, 2.04, and 1.44 Å. These, on correlation with the literature values, are found to match with those of Pt(111), Pt(200), and Pt(220) planes, respectively. Moreover, XRD peaks (Figure 2)

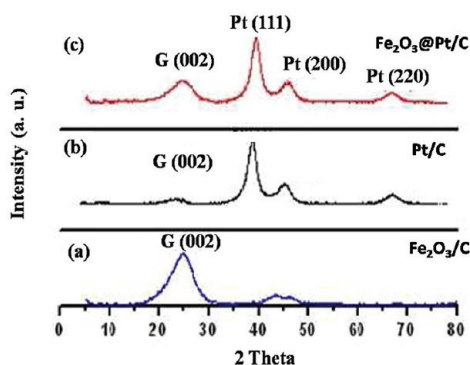


**Figure 2.** XRD pattern (a)  $\text{Fe}_2\text{O}_3/\text{C}$ , (b)  $\text{Pt}/\text{C}$ , and (c)  $\text{Fe}_2\text{O}_3@\text{Pt}/\text{C}$ .

obtained at  $43^\circ$  and  $47^\circ$ , corresponding to the iron oxide phase of  $\text{Fe}_2\text{O}_3/\text{C}$ , vanish in the case of  $\text{Fe}_2\text{O}_3@\text{Pt}/\text{C}$  and instead well-distinguished peaks at  $39.8^\circ$ ,  $46.4^\circ$ , and  $68.6^\circ$ , corresponding to the (111), (200), and (220) planes of the fcc crystal of Pt, appear. In addition, the clear shift of the XRD peaks toward higher  $2\theta$  value of Pt(111) certifies the lattice contraction, which indicates the change in the electronic as well as geometric nature and confirms the implications from the TEM observations as discussed above. The broad peaks in the XRD pattern presumably indicate the high dispersion of the nanoparticles possessing small particle sizes on the substrate surface.

As mentioned earlier, to maintain better dispersion of the core–shell nanoparticles, both AA and its oxidative products formed during the synthesis process create the anchoring sites on the carbon surface and, thus, effectively prevent agglomeration of the particles on the substrate surface. The formation of the functional groups on the surface of the carbon substrate has been confirmed by IR spectroscopy. Figure 3

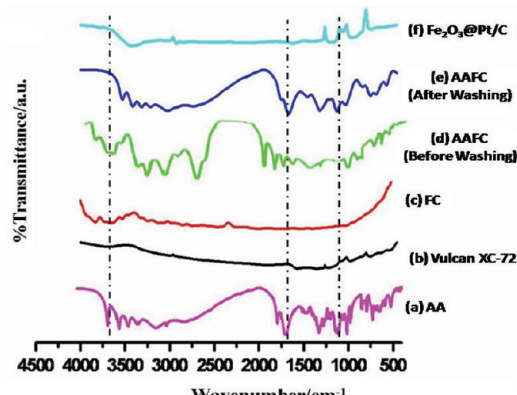


**Figure 3.** IR spectra of (a) ascorbic acid (AA), (b) Vulcan XC-72, (c) functionalized carbon (FC), (d, e) AA-treated FC (AAFC) (before washing and after washing), and (f)  $\text{Fe}_2\text{O}_3@\text{Pt}/\text{C}$ .

shows the IR spectra of AA, Vulcan XC-72, Vulcan XC-72 functionalized by hydrogen peroxide (FC), and AA-treated FC (AAFC) before and after washing and after core–shell nanoparticles dispersion on AAFC. The IR band at  $\sim 1745 \text{ cm}^{-1}$  of the AAFC is corresponding to the carbonyl stretching frequency of the dehydroascorbic acid and 2,3-diketogulonic acid moieties grafted during the reduction process. Furthermore, the peaks at  $\sim 1055$  and  $\sim 1225 \text{ cm}^{-1}$  are attributed to the C–O stretching of acid and ether groups, respectively. These IR stretching gives confirmation on the in situ modification of the support surface. The analysis also reveals that dispersion of  $\text{Fe}_2\text{O}_3@\text{Pt}/\text{C}$  nanoparticles on the carbon support surface eradicates the majority of the surface groups grafted on the surface. The coexistence of the reduction products and the oxidized and decomposed intermediates along with the excess reducing agent and provision for direct anchoring on the substrate surface thus ensure a quality dispersion by effectively preventing extensive growth of the particles. Overall, the process leads to the conceptualization of ex situ dispersion of core–shell nanoparticles on in situ modified carbon substrate in the reaction mixture where the particles are actually originated. In this way, many multistep processes and postsynthesis treatments could be effectively eliminated, which often trigger aggregation of particles and inhomogeneity in their dispersions.

The change in the electronic environment has also been confirmed by XPS analysis. Figure 4 shows the deconvoluted XPS spectra of Fe and Pt in  $\text{Fe}_2\text{O}_3@\text{Pt}/\text{C}$ . Figure 4ii shows the comparative XPS spectra of pure Pt and Pt of the core–shell nanoparticles. The Pt 4f spectrum of the core–shell material is fitted with four peaks originating from the spin–orbit splitting of  ${}^4\text{f}_{7/2}$  and  ${}^4\text{f}_{5/2}$  states. The peaks at the binding energy of  $\sim 71.3$  (Pt ${}^4\text{f}_{7/2}$ ) and  $\sim 74.5 \text{ eV}$  (Pt ${}^4\text{f}_{5/2}$ ) are attributed to the Pt $^0$  state, whereas the two supplementary peaks at the binding energy of  $\sim 72.8$  and  $\sim 76.6 \text{ eV}$  are attributed to the Pt $^{2+}$  state. A comparison of the relative intensities of the peaks due to Pt $^0$  and those of Pt–O shows that Pt in both the catalysts is predominately metallic. However, the higher binding energy of the Pt peaks comparing to the pure Pt can be attributed to the core and shell interface and the small size of the Pt, which lead to the bonding between O and Pt and bring alteration in its electronic structure.<sup>8,12</sup> The delocalized electrons in the p-orbital of the  $\pi$ -sites on carbon overlap with a d-orbital of Pt, signifying that the nature of bonding is partially covalent.<sup>13</sup> Moreover, the XPS data of pure Pt (Figure 4ii) shows only two peaks without any supplementary peaks at the binding energies of 71.0 and 74.1 eV corresponding to the Pt $^0$  state. Absence of the peaks corresponding to the Pt–O indicates that Pt in this system is purely metallic. A shift in the Pt peaks of core–shell nanoparticles and appearance of two more supplementary peaks confirm the O and Pt bonding. XPS of Fe shows peaks at 709.7 and 724.11 eV which are attributed to Fe $^0$  ( ${}^2\text{p}_{3/2}$ ,  ${}^2\text{p}_{1/2}$ ). There are also peaks at 712 and 725.6 eV along with a satellite peak at  $\sim 718 \text{ eV}$ , which indicate the bonding of Fe with oxygen.<sup>14</sup> This indicates that the core is having a mixed composition of both metallic and oxidic characteristics, even though the oxide phase predominates over the metallic phase. The combined XPS spectra of  $\text{Fe}_2\text{O}_3@\text{Pt}/\text{C}$  are presented in the Supporting Information (Figure S3). Further, to investigate the thermal stability of the catalysts, thermogravimetric analysis (TGA) has been done in an N<sub>2</sub> atmosphere (Supporting Information, Figure S4). TGA plots of the commercial Pt/C,  $\text{Fe}_2\text{O}_3/\text{C}$ , and  $\text{Fe}_2\text{O}_3@\text{Pt}/\text{C}$  show an initial weight loss at 100 °C, which can be attributed to the loss of moisture. Further loss

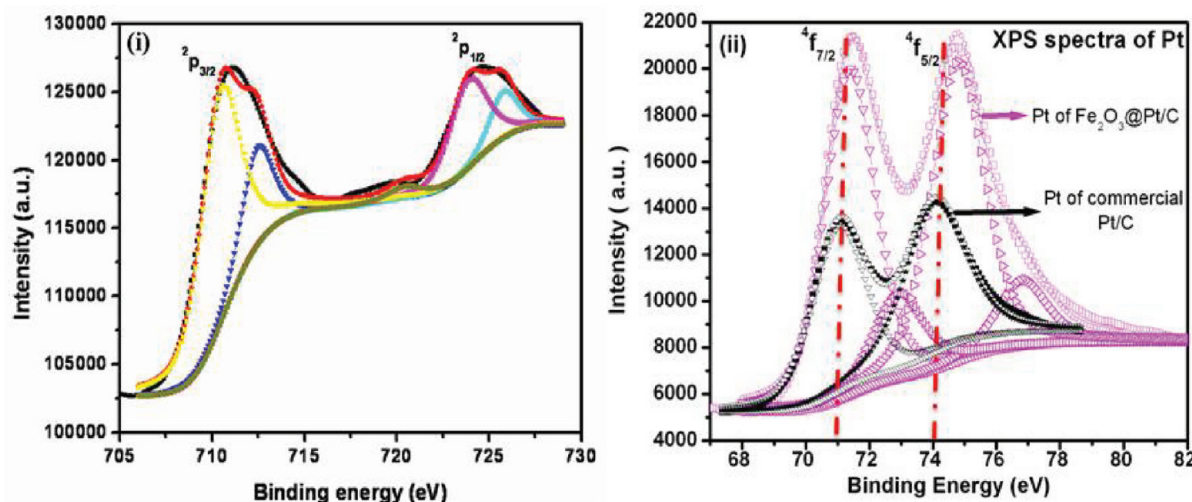


Figure 4. Deconvoluted XPS spectra of (i)  $\text{Fe}_2\text{O}_3$ , (ii) Pt of  $\text{Fe}_2\text{O}_3@\text{Pt/C}$  (pink), and pure Pt (black).

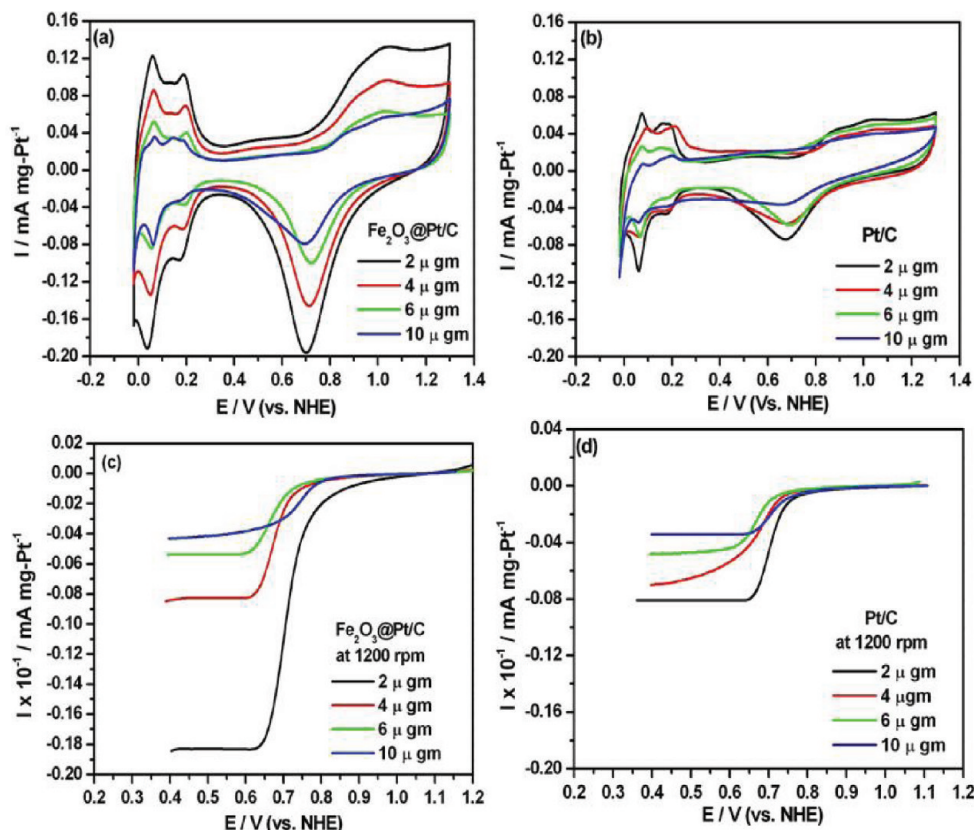


Figure 5. Combined cyclic voltammograms of (a)  $\text{Fe}_2\text{O}_3@\text{Pt/C}$ , (b) Pt/C with different Pt loadings performed at 100 mV/s in 0.5 M perchloric acid, and the LSV of (c)  $\text{Fe}_2\text{O}_3@\text{Pt/C}$  and (d) Pt/C performed at 1200 rpm with a scan rate of 10 mV/s in an oxygen atmosphere. All the graphs are corrected with the ohmic losses and are normalized with respect to NHE.

in the weight starting at 400 °C is due to the decomposition of carbon. A residual weight of 64 wt % in the case of  $\text{Fe}_2\text{O}_3@\text{Pt/C}$  core–shell catalyst indicates the combined weight of Pt, Fe, and the corresponding oxide forms of Fe.

Electrochemical evaluation of the samples further augments the formation of the core–shell structure with the modulated electronic and structural properties as visualized from the aforementioned characterization data. This has been confirmed by a set of dedicated electrochemical experiments. Parts a and b of Figure 5 respectively show the cyclic voltammograms of

$\text{Fe}_2\text{O}_3@\text{Pt/C}$  and Pt/C with different Pt loadings on the electrode at a scan rate of 100 mV/s in 0.5 M perchloric acid with a conventional three-electrode system. The hydrogen adsorption and desorption take place in the potential range of 0–0.3 V (vs NHE), and the features in this region resemble very much that of a polycrystalline Pt electrode in acid solution. The absence of the redox couple corresponding to the Fe moiety clearly underlines the formation of a continuous protective layer of Pt over the iron-based core (Supporting Information, Figure S2).<sup>15</sup> The core and shell are mutually

benefitted and they together bring integrity and efficiency. As the protective case of Pt ensures the required electrochemical stability of the core in the operating potential window, the morphology and surface roughness of the core on the other hand dictate Pt growth and thereby its unprecedentedly high active surface area is attained. The electrochemically active surface area (ECSA) has been calculated from the charge required for hydrogen desorption by using the formula

$$\text{ECSA} = \frac{Q_{\text{H}} mC}{0.21mC \times \text{Pt loading (mg cm}^{-2}\text{)}}$$

where,  $Q_{\text{H}}$  is the charge for hydrogen desorption and  $0.21mC$  represents the charge required to oxidize a monolayer of H from the surface of Pt.<sup>16</sup> An important behavior that we observed while measuring the ECSA of the core–shell catalyst is its relatively high sensitivity to the coating thickness on the electrode surface compared to the normal Pt/C catalyst. The measured ECSA values as a function of the catalyst loading on the electrode for  $\text{Fe}_2\text{O}_3@\text{Pt/C}$  follows the order  $185 \text{ m}^2/\text{g}$  ( $2 \mu\text{g}$ )  $> 140 \text{ m}^2/\text{g}$  ( $4 \mu\text{g}$ )  $> 122 \text{ m}^2/\text{g}$  ( $6 \mu\text{g}$ )  $> 102 \text{ m}^2/\text{g}$  ( $10 \mu\text{g}$ ). Even though Pt/C also displayed a similar trend for its ECSA with the loading amount as  $119 \text{ m}^2/\text{g}$  ( $2 \mu\text{g}$ )  $> 118 \text{ m}^2/\text{g}$  ( $4 \mu\text{g}$ )  $> 107 \text{ m}^2/\text{g}$  ( $6 \mu\text{g}$ )  $> 87 \text{ m}^2/\text{g}$  ( $10 \mu\text{g}$ ), a notable drop in this case has been observed only when the coating thickness goes to a significantly high level. It should also be noted that the ECSAs of  $\text{Fe}_2\text{O}_3@\text{Pt/C}$  are distinctly ahead of Pt/C under low catalyst loading conditions. Figure S5 (Supporting Information) depicts the comparative CV with different Pt loadings. The calculated ECSA values are plotted in Figure S6 (Supporting Information), which clearly highlights the need to look into the optimum loading of the electrocatalyst to effectively make use of the morphological and structural benefits of the core–shell material. The high sensitivity of the  $\text{Fe}_2\text{O}_3@\text{Pt/C}$  catalyst with its coating amount on the electrode can be attributed to the resistance imposed by the core material, which increases significantly owing to its high mass fraction compared to Pt in the system. This is an important observation in the context of developing MEAs for PEMFCs, because as can be evident from later discussions, the best performance characteristics of an electrode derived from the  $\text{Fe}_2\text{O}_3@\text{Pt/C}$  catalyst could be obtained only when the thickness of the electrode was maintained below a threshold level. Moreover, the durability assessment of  $\text{Fe}_2\text{O}_3/\text{C}$  and  $\text{Fe}_2\text{O}_3@\text{Pt/C}$  (Supporting Information, Figure S2d,e) catalyst has been done by subjecting potential cycling (100 cycles) between 0 and 1.3 V (vs NHE). A potential cycling can provide very useful information on the leaching of the iron-based core under acidic conditions if the core is not well protected by the Pt shell. This is a relatively fast and reliable method to confirm the formation of a protective layer of Pt on the base metal like Fe. Since the core–shell structure has been confirmed from TEM, XRD, and CV, the absence of anodic peaks of iron-based core in  $\text{Fe}_2\text{O}_3@\text{Pt/C}$  indicates the incessant shell of Pt on the surface of the iron-based core (Supporting Information, Figure S2).

On par with the ECSA measurements, an analysis of the ORR activity also reveals a strong dependency on the coating thickness (Figures 5c,d and S7, Supporting Information). The electrocatalytic activities for ORR are recorded by the hydrodynamic RDE technique at different rotation speeds per minute (rpm). A huge difference in the performance characteristics between the two catalysts is clearly visible when the catalyst loading was maintained as  $2 \mu\text{g}$  on the electrode. The

enhanced activity of  $\text{Fe}_2\text{O}_3@\text{Pt/C}$  can be ascribed to the multiple features such as high ECSA, electronic modifications, and synergistic effects enjoyed by the system all the while avoiding the chance for the ohmic component of the core material to dominate and consequently upset the expected improvement in performance. The literature<sup>17,18</sup> shows that addition of a second metal exhibits an increase of surface d-vacancy, which facilitates electron donation from oxygen to the surface Pt. This brings strong interaction between Pt and oxygen, which results in enhancement of oxygen adsorption and weakening of the O–O bond, leading to fast scission of the bond and enhanced ORR activities.<sup>8,9,17,18</sup>

As already seen, the ORR activity of the core–shell catalyst, just like ECSA, is found to be significantly influenced by the coating amount of the catalyst on the electrode. A combined set of RDE polarization curves performed at 1200 rpm as a function of the coating amount of the catalyst on the electrode, as shown in parts c and d of Figure 5 for  $\text{Fe}_2\text{O}_3@\text{Pt/C}$  and Pt/C respectively sheds light into the fact that, unless the coating thickness is maintained within a threshold level, the benefits expected from the core–shell morphology cannot be extracted effectively. It should be noted that the compositional effect and loading effect together dictate the ORR activity even though the extent of domination of the factors varies with the coating levels. Under low loading conditions, the core–shell system enjoys a clear edge over Pt/C in terms of both ECSA and ORR activity, whereas the differences narrow down as the coating thickness increases. The large mass fraction of the core material, which is predominantly oxidic, makes significant ohmic overpotential contribution and clearly dictates the performance under higher loading conditions. This important observation should not be underestimated during electrode fabrication because the real performance benefits of the core–shell materials with oxide cores may not be clearly visualized beyond a coating thickness owing to the dominating role played by the ohmic component of the core materials.

Further insights into the ORR dynamics were obtained from the analysis of the Koutecky–Levich (K-L) plot at 0.45 V, which is a plot of the inverse of current density ( $J^{-1}$ ) as a function of the inverse of the square root of the rotation rate ( $\omega^{-1/2}$ ), as shown in Figure 6. Total current obtained in the

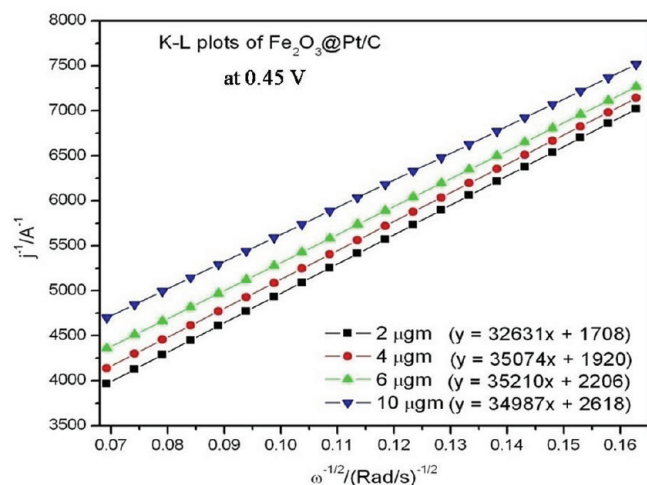


**Figure 6.** Koutecky–Levich plots of  $\text{Fe}_2\text{O}_3@\text{Pt/C}$  at 0.45 V generated from the LSVs taken as a function of different catalyst loading amounts.

analysis is the sum of the inverse of diffusion, kinetic and film diffusion currents. However, in the present case, as the amount of Nafion is significantly low, the film diffusion current component can be neglected.<sup>19</sup> Therefore, in the laminar flow region, the diffusion current density is a function of the rotational velocity and hence the kinetic current densities can be adjusted to the simple K-L equation as follows:

$$\frac{1}{J} = \frac{1}{nFkC_{O_2}} + \frac{1}{0.62nFAC_{O_2}D_{O_2}^{2/3}\nu^{-1/6}\omega^{1/2}}$$

where  $J$  is the disk electrode current density,  $k$  is the reaction rate constant,  $n$  is the number of electrons exchanged per  $O_2$  molecule,  $F$  is the Faraday constant,  $A$  is the electrode geometric area ( $0.07\ 065\ cm^2$ ),  $C_{O_2}$  is the bulk oxygen concentration ( $1.22 \times 10^{-6}\ mol/cm^3$ ),  $D_{O_2}$  is the diffusion coefficient of molecular oxygen ( $1.93 \times 10^{-5}\ cm^2/s$ ),  $\nu$  is the kinematic viscosity of the electrolyte ( $0.0913\ cm^2/s$ ), and  $\omega$  is the angular rotation of electrode in radians per second ( $=2\pi f = 2\pi\ rpm\ number/60$ ). This equation gives a linear relation between  $J^{-1}$  and  $\omega^{-1/2}$  with a Y-intercept equal to the inverse of the kinetic current density ( $j_k^{-1}$ ). The corresponding K-L plots generated from  $Fe_2O_3@Pt/C$  at different coating thicknesses are shown in Figure 6. Good linearity and parallelism of the K-L plots indicate that ORR follows first-order kinetics and similar mechanistic aspects.<sup>20</sup> The reaction proceeds via a four-electron transfer, which has been calculated from a Levich plot analysis of the RDE data. The calculated kinetic current density ( $j_k$ ) for the core–shell catalyst is  $5.8 \times 10^{-4}\ A/cm^2$  when the catalyst loading was maintained as  $2\ \mu g$ . On the other hand, in the case of  $Pt/C$ , the same catalyst loading gives a lower  $j_k$  value of  $3.8 \times 10^{-4}\ A/cm^2$ . However, it has been noticed that the difference between the two systems in terms of the measured  $j_k$  values narrows down as the catalyst coating thickness increases. This clearly indicates that the ORR kinetics of the core–shell catalyst is clearly higher than that of the conventional  $Pt/C$  catalyst, provided the thickness of the catalyst layer does not exceed a threshold level. The obtained higher activity at low Pt loading is attributed to the low resistance and better internal diffusion of the reactant at low thickness level. Overall, it was found from the results that the ORR activity can be affected by the contributions from ohmic and diffusion components, and the ohmic component appears to play a dominating role in the case of the core–shell system owing to the large mass fraction of the core component whose conductivity is expected to be significantly lower than that of Pt.

Further to investigate more clearly the effect of loading and thickness in a realistic perspective, we carried out a series of single cell performance evaluation with varying cathode Pt loading from  $0.05$  to  $0.2\ mg/cm^2$  (Figure 7). The thickness of the Pt-coated gas diffusion layer with varying Pt loading has been measured by the SEM analysis, and the corresponding images are shown in Figure S1 (Supporting Information). The analysis reveals that the thickness of the electrode possessing the Pt loading of  $0.05\ mg/cm^2$  is approximately  $19.5\ \mu m$  and this increases significantly (nearly to  $90\ \mu m$ ) as the Pt loading goes to  $0.2\ mg/cm^2$ . It should be noted that the variation in the Pt loading has been achieved by controlling the catalyst coating thickness on the electrode. The trend in performance during the single cell evaluation is on par with the RDE results with respect to the thickness effect. The MEA corresponding to the cathode Pt loading of  $0.05\ mg/cm^2$ , i.e., the one with the lowest thickness, displays the highest power density of  $900\ mW/cm^2$ ,

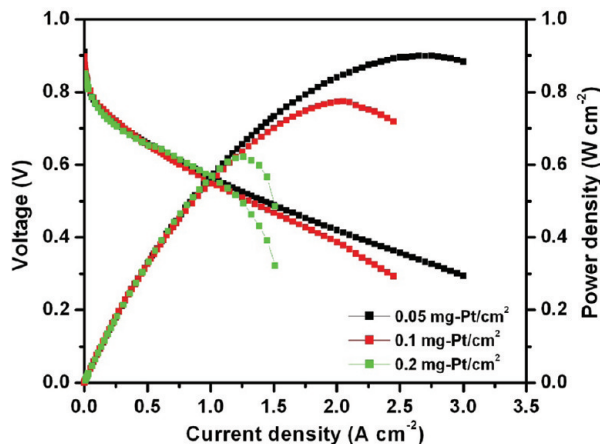


**Figure 7.** Polarization plots of MEAs fabricated by using  $Fe_2O_3@Pt/C$  with different Pt loadings by passing ultrapure  $H_2$  and  $O_2$  at anode and cathode sides respectively at a flow rate of  $0.2\ slpm$  (100% relative humidity and at  $60\ ^\circ C$  cell temperature).

whereas the MEA prepared by  $Pt/C$  with the same Pt loading and under similar test conditions displays a power density of approximately  $700\ mW/cm^2$  (Supporting Information, Figure S9). One reason for the high performance at low loading for  $Fe_2O_3@Pt/C$  can be attributed to the higher ECSA of the core–shell structure, which is better accessible when the coating thickness of the electrode is low. As the thickness increases above a threshold level, along with the expected mass transfer effects, the resistance contribution from the base metal species can be dominated in the core–shell system unlike in a  $Pt/C$ -based electrode. This leads to a technical limitation in obtaining the expected benefits from the core–shell geometry of thicker electrodes. Further, to understand the kinetics of the fuel cell reaction, the exchange current density has been calculated from the Tafel plot. The Tafel slope is an indication of the mechanism of the electrode reaction, which is related to the change in the nature of adsorbed oxygen species and their coverage variation with the potential. The low current density region corresponds to the oxygen reduction when the adsorbed hydroxyl species at the Pt surface determines the electrode activity. Tafel plot has been created by measuring the in situ resistance during actual single cell testing and making accordingly the required IR compensation in the measured voltage. Both Tafel intercept and slope have been used to reveal the properties of the rate-determining step. Figure 9 shows representative comparative Tafel plots generated from the single cell polarization data based on the electrodes fabricated from  $Fe_2O_3@Pt/C$  and  $Pt/C$ . The measured Tafel slope values are  $61\ mV/decade$  for the core–shell system and  $72\ mV/decade$  for the  $Pt/C$  system. The Tafel slope can then be used to calculate the effective transfer coefficient, and the Tafel intercept gives the value of exchange current density. The calculated transfer coefficient ( $\alpha$ ) is nearly  $0.5$  for both the systems. However, more than 1 order of the difference in the exchange current density as measured for  $Fe_2O_3@Pt/C$  ( $1.26 \times 10^{-7}\ A/cm^2$ ) and  $Pt/C$  ( $6.60 \times 10^{-8}\ A/cm^2$ ) clearly depicts the distinct benefit obtainable from a properly designed electrode based on the core–shell catalyst for PEMFC applications. Durability of MEAs has been tested for  $10\ h$  (Figure 8) by keeping the cell at  $0.6\ V$  for  $30\ min$  and thereafter switching the voltage to OCV and again bringing it back to  $0.6\ V$ . We found that there is little fluctuation in potential, but the current

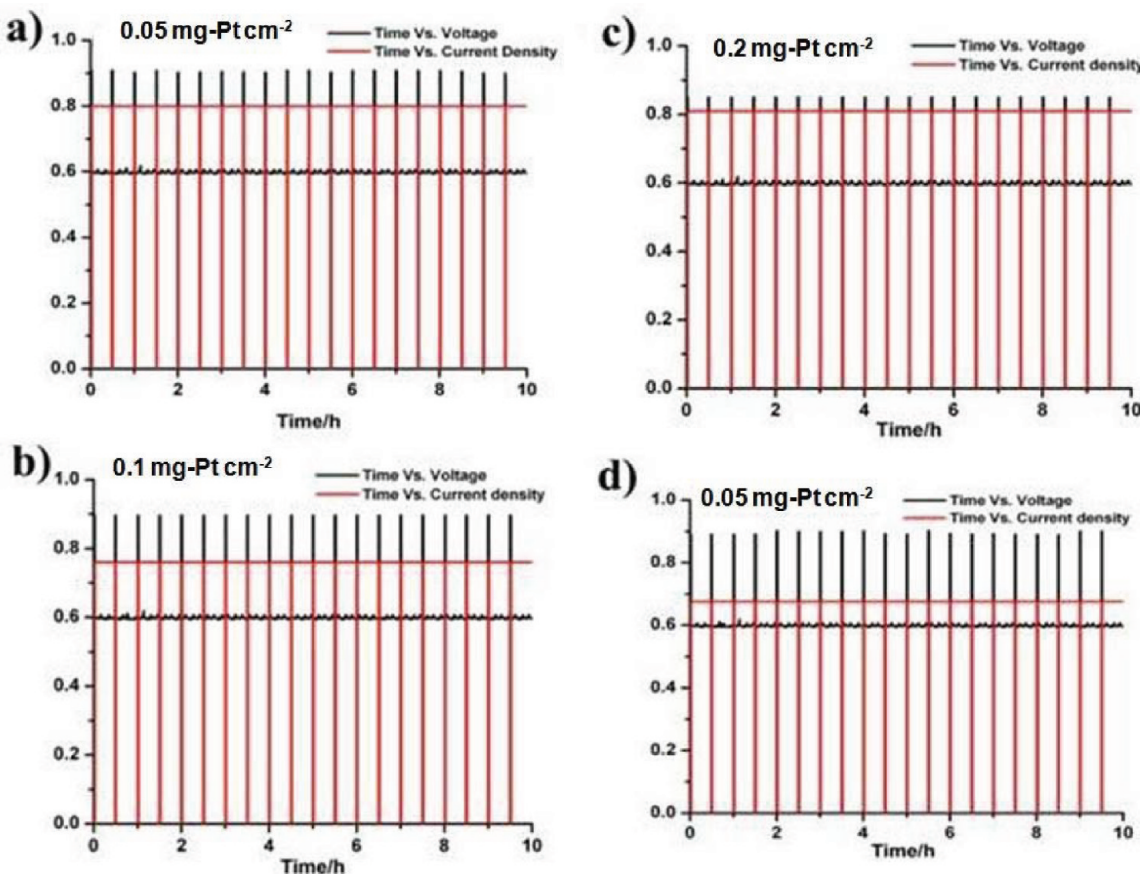


**Figure 8.** Durability study of the MEAs by switching the voltage between 0.6 V and OCV (10 h) by passing ultrapure H<sub>2</sub> and O<sub>2</sub> on the anode and cathode sides, respectively. Fe<sub>2</sub>O<sub>3</sub>@Pt/CMEA having (a) 0.05 mg of Pt/cm<sup>2</sup>, (b) 0.1 mg of Pt/cm<sup>2</sup>, and (c) 0.2 mg of Pt/cm<sup>2</sup> loading at the cathode side. (d) MEA prepared by Pt/C having 0.05 mg of Pt/cm<sup>2</sup> loading at the cathode side. In all the cases, the anode side Pt loading was maintained as 0.3 mg/cm<sup>2</sup>.

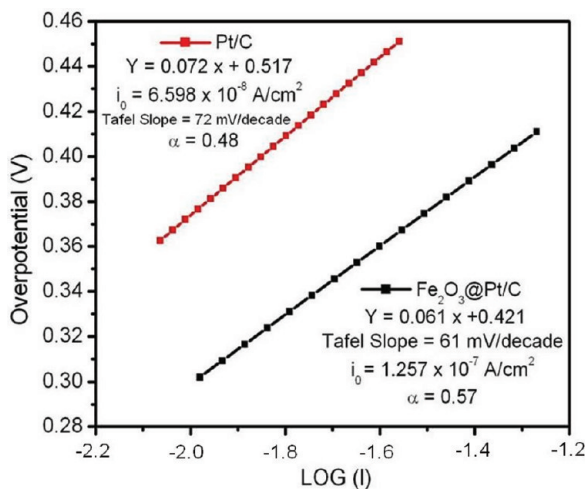


**Figure 9.** Comparative Tafel plots of Pt/C and Fe<sub>2</sub>O<sub>3</sub>@Pt/C derived from the single cell analysis.

density is constant throughout the evaluation period of 10 h. The obtained results are tabulated in Table 1. Thus the durability assessment assures the integrity of the core–shell material and reliability of the electrodes derived from these materials to deliver sustainable power output (voltage × current) under the operating electrochemical environments.

**Table 1. Electrochemical Activities of the Prepared Catalysts and Their Single Cell Performance Data**

	Electrochemical Active Surface Area (m <sup>2</sup> /g)			
	2 µg of Pt	4 µg of Pt	6 µg of Pt	10 µg of Pt
Fe <sub>2</sub> O <sub>3</sub> @Pt/C	185	140	122	102
Pt/C	119	118	107	87
Single Cell Performance Evaluation				
Fe <sub>2</sub> O <sub>3</sub> @Pt/C				
cathode Pt loading (mg cm⁻²)	max. power density (mW/cm²)	max. current density (mA/cm²)	OCV (V)	
0.05	900	3000	0.91	
0.1	775	2450	0.896	
0.2	622	1510	0.85	

#### 4. CONCLUSIONS

Fe<sub>2</sub>O<sub>3</sub>@Pt/C electrocatalyst possessing core–shell nanoparticle dispersion on the carbon substrate has been synthesized by a sequential reduction method, using ascorbic acid as the reducing agent and by completely eliminating any capping agent. Both core–shell feature and high particle dispersion on the active carbon surface could be simultaneously maintained by the adopted surface modification-cum-anchoring strategy. Consequently, this led to a high-performance electrocatalyst for oxygen reduction reaction at a significantly low Pt loading, which could not be realized by the conventional approaches. However, in a system possessing a less conductive core

material, i.e.  $\text{Fe}_2\text{O}_3$ , it is mandatory to prevent the electrode thickness from exceeding a threshold level owing to the greater dominance of the core material with its higher mass fraction in the system. Exceeding the thickness beyond a threshold level upsets the electrochemically active surface area, oxygen reduction kinetics, and polarization characteristics. On the other hand, in properly optimized systems, the core–shell material clearly outperforms the conventional Pt-based electrocatalyst, leaving great scope for the development of high-performance, cost-effective low-Pt electrocatalysts possessing excellent electrochemical stability. Realization of high-performance thin electrodes is expected to make radical changes in the design aspects of PEMFCs along with its potential to develop miniature cells for various niche applications. This could be an innovative and elegant solution for realizing micro fuel cells and better system adaptability for various applications.

## ASSOCIATED CONTENT

### Supporting Information

SEM images of electrode, durability data of  $\text{Fe}_2\text{O}_3/\text{C}$  and  $\text{Fe}_2\text{O}_3@\text{Pt/C}$ , thermogravimetric data, and I–V curve of Pt/C with 0.05 mg of  $\text{Pt}/\text{cm}^2$  loading. This material is available free of charge via the Internet at <http://pubs.acs.org>.

## AUTHOR INFORMATION

### Corresponding Author

\*Fax: +91-20-25902636. Tel: +91-20-25902566. E-mail: k.sreekumar@ncl.res.in.

### Notes

The authors declare no competing financial interest.

## ACKNOWLEDGMENTS

This study was financially supported by Council of Scientific and Industrial Research (CSIR), India, under the Network Project No. NWP0022. The authors thank Dr. Sourav Pal and Dr. Sivaram for their constant support, CSIR for the financial assistance, and Dr. K. Vijayamohanan for the valuable discussions. The authors also thank Mr. Narendra and Mr. Pandiaraj for providing TEM images.

## REFERENCES

- (1) (a) Barbir, F. *PEM Fuel Cells: Theory and Practice*; Elsevier: San Diego, CA, 2005. (b) Carrette, L.; Friedrich, K. A.; Stimming, U. *Fuel Cells—Fundamentals and Applications*. *Fuel Cells* **2001**, *1* (1), 5–39.
- (c) Lim, B.; Jiang, M.; Camargo, P. H. C.; Cho, E. C.; Tao, J.; Lu, X.; Zhu, Y.; Xia, Y. *Science* **2009**, *324*, 1302–1305. (b) Shao, M.-H.; Sasaki, K.; Adzic, R. R. *J. Am. Chem. Soc.* **2006**, *128*, 3526–3527. (c) Gong, K.; Du, F.; Xia, Z.; Durstock, M.; Dai, L. *Science* **2009**, *323*, 760.
- (2) Shih, Y.-H.; Sagar, G. V.; Lin, S. D. *J. Phys. Chem. C* **2008**, *112*, 123–130.
- (3) Mark, K. D.; et al. Advanced Cathode Catalysts and Supports for PEM Fuel Cells. In *FY 2009 Progress Report for the DOE Hydrogen Program*; U.S. Department of Energy: Washington, DC, 2009; p 1065.
- (4) (a) Kariuki, N. N.; Wang, X.; Mawdsley, J. R.; Ferrandon, M. S.; Niyogi, S. G.; Vaughtey, J. T.; Myers, D. *J. Chem. Mater.* **2010**, *22*, 4144–4152. (b) Sinfelt, J. H. *Bimetallic Catalysts: Discoveries, Concepts and Applications*; John Wiley & Sons: London, 1983. (d) Maroun, F.; Ozanam, F.; Magnussen, O. M.; Behm, R. J. *Science* **2001**, *293*, 1811–1814.
- (5) Beard, K. D.; Borrelli, D.; Cramer, A. M.; Blom, D.; Van Zee, J. W.; Monnier, J. R. *ACS Nano* **2009**, *3*, 2841.
- (6) Strasser, P.; Koh, S.; Anniyev, T.; Greeley, J.; More, K.; Yu, C.; Liu, Z.; Kaya, S.; Nordlund, D.; Ogasawara, H.; Toney, M. F.; Nilsson, A. *Nat. Chem.* **2010**, *2*, 454–460.
- (7) Kitchin, J. R.; Norskov, J. K.; Bartea, M. A.; Chen, J. G. *Phys. Rev. Lett.* **2004**, *93*, 156801–156804.
- (8) Hwang, S. J.; Yoo, S. J.; Jang, S.; Lim, T.-H.; Hong, S. A.; Kim, S.-K. *J. Phys. Chem. C* **2011**, *115*, 2483–2488.
- (9) (a) Min, M.-K.; Cho, J. H.; Cho, K. W.; Kim, H. *Electrochim. Acta* **2000**, *45*, 4211. (b) Stamenkovic, V. R.; Mun, B. S.; Arenz, M.; Mayrhofer, K. J.; Lucas, C. A.; Wang, G.; Ross, P. N.; Markovic, N. M. *Nat. Mater.* **2007**, *6*, 241–247.
- (10) Dhavale, V. M.; Unni, S. M.; Kagalwala, H. N.; Pillai, V. K.; Kurungot, S. *Chem. Commun.* **2011**, *47*, 3951–3953.
- (11) Deshmukh, A. B.; Kale, V. S.; Dhavale, V. M.; Sreekumar, K.; Vijayamohanan, K.; Shelke, M. V. *Electrochim. Commun.* **2010**, *11*, 1638–1641.
- (12) Arico, A. S.; Srinivasan, S.; Antonucci, V. DMFCs: From Fundamental Aspects to Technology Development. *Fuel Cells* **2001**, *1*, 133.
- (13) Cuong, N. T.; Chi, D. H.; Kim, Y.-T.; Mitani, T. *Phys. Status Solidi* **2006**, *13*, 3472.
- (14) Moulder, J. F.; Stickle, W. F.; Sobol, P. E.; Bomben, K. D. *Handbook of X-ray Photoelectron Spectroscopy: A Reference Book of Standardized Spectra for Identification and Interpretation of XPS Data*; Physical Electronics, Division, Perkin-Elmer Corp.: Eden Prairie, MN, 1995.
- (15) Jayasayee, K.; Dam, V. A. T.; Verhoeven, T.; Celebi, S.; de Brujin, F. A. *J. Phys. Chem. C* **2009**, *113*, 20371–20380.
- (16) Pozio, A.; De Francesco, M.; Cemmi, A.; Cardellini, F.; Giorgi, L. *J. Power Sources* **2002**, *105*, 13.
- (17) Toda, T.; Igarashi, H.; Uchida, H.; Watanabe, M. *J. Electrochem. Soc.* **1999**, *146*, 3750–3756.
- (18) Okada, T.; Abe, T.; Kaneko, M. *Molecular Catalyst for Energy Conversion*; Springer Series in Material Science 111; Springer-Verlag: Berlin, 2009.
- (19) Bard, A. J.; Faulkner, L. R. *Electrochemical Methods Fundamentals and Applications*, 2nd ed.; John Wiley & Sons, Inc.: New York, 2006.
- (20) Wroblowa, H. S.; Qaderi, S. B. *J. Electroanal. Chem.* **1990**, *279*, 2314–242.
- (21) He, P.; Faulkner, L. R. *Anal. Chem.* **1986**, *58*, 517–523.